Layer and material-type dependent photoresponse in WSe_2/WS_2 vertical heterostructures

2D Materials

PAPER

RECEIVED
29 October 2021

REVISED
22 November 2021

ACCEPTED FOR PUBLICATION
23 November 2021

PUBLISHED
7 December 2021

Layer and material-type dependent photoresponse in WSe_2/WS_2 vertical heterostructures

ZhuangEn Fu[1,4], Josh W Hill[2,4], Bruce Parkinson[2,3], Caleb M Hill[2,*] and Jifa Tian[1,*]

[1] Department of Physics & Astronomy, University of Wyoming, Laramie, WY 82071, United States of America
[2] Department of Chemistry, University of Wyoming, Laramie, WY 82071, United States of America
[3] School of Energy Resources, University of Wyoming, Laramie, WY 82071, United States of America
[4] These authors contributed equally.
[*] Authors to whom any correspondence should be addressed.

E-mail: caleb.hill@uwyo.edu **and** jtian@uwyo.edu

Keywords: WSe_2, WS_2, transition metal dichalcogenide heterostructure, scanning electrochemical cell microscopy, photovoltaic effect

Supplementary material for this article is available online

Abstract

Transition metal dichalcogenide (TMD) heterostructures are promising for a variety of applications in photovoltaics and photosensing. Successfully exploiting these heterostructures will require an understanding of their layer-dependent electronic structures. However, there is no experimental data demonstrating the layer-number dependence of photovoltaic effects (PVEs) in vertical TMD heterojunctions. Here, by combining scanning electrochemical cell microscopy (SECCM) with optical probes, we report the first layer-dependence of photocurrents in WSe_2/WS_2 vertical heterostructures as well as in pristine WS_2 and WSe_2 layers. For WS_2, we find that photocurrents increase with increasing layer thickness, whereas for WSe_2 the layer dependence is more complex and depends on both the layer number and applied bias (V_b). We further find that photocurrents in the WSe_2/WS_2 heterostructures exhibit anomalous layer and material-type dependent behaviors. Our results advance the understanding of photoresponse in atomically thin WSe_2/WS_2 heterostructures and pave the way to novel nanoelectronic and optoelectronic devices.

1. Introduction

Transition metal dichalcogenides (TMDs) (such as MoS_2, $MoSe_2$, WS_2, and WSe_2) are promising candidate materials for nanoelectronics and optoelectronics [1–13], owing to their strong light-matter interactions [1] and layer-dependent electronic structures [13, 14]. The ability to precisely fabricate vdW heterostructures [15] by assembling different TMD atomic layers provides a novel route to a wide variety of artificial semiconductor heterostructures and Moiré superlattices [16–18]. Furthermore, the thickness-dependent band gaps of thin TMD layers enable even more possibilities to create novel p–n junctions at the atomic scale for photodetection and energy-harvesting applications [19]. In the past few years, most efforts have been devoted to exploring the photoresponse in heterojunctions made of different TMD monolayers or their multilayers with random thicknesses, such as WSe_2/MoS_2 [19, 20], black *phosphorene*/MoS_2 [21, 22], $MoTe_2/MoS_2$ [23, 24], WSe_2/SnS_2 [25, 26]. On the other hand, for solar cell applications, it has been shown that the responsivity can be significantly enhanced in vertical heterojunctions consisting of TMD multilayers [19, 27]. However, due to the technical difficulties associated with the fabrication of top and bottom electrical contacts and the relatively low spatial resolution achievable with current laser-based techniques, little work has been performed to study the layer dependence of the photovoltaic effects (PVEs) in TMD-based heterojunctions, particularly along the vertical direction, thus far. To fully explore the potential of TMD-based vdW heterostructures for future energy-harvesting applications, studies of the layer-dependent photoresponse in TMD heterojunctions are highly desirable.

In this paper, we report the preparation of high-quality, atomically thin layers of WS_2 (intrinsic), WSe_2 (p-type) and their vertical heterojunctions on conductive indium tin oxide (ITO) substrates. We

employed a unique tool, scanning electrochemical cell microscopy (SECCM) [28–36] to study the PVEs of the prepared TMD layers along the out-of-plane direction. We systematically studied the layer-dependent PVEs of the pristine WS_2 and WSe_2 atomic layers as well as their heterostructures. In addition, we show the strong layer-dependent PL of the corresponding pristine WS_2 and WSe_2 atomic layers and their heterostructures. Our results indicate that the atomically thin WSe_2/WS_2 heterostructures with type-II band alignment and distinct layer- and material type dependent photocurrent generation characteristics can be used to create novel nanoelectronic and optoelectronic devices.

2. Results and discussion

2.1. Layer-dependent PL and PVE of WS_2

Figure 1(a) shows a representative optical image of the pristine WS_2 atomic layers prepared on an ITO substrate using the dry transfer technique [37] (see figure S1 available online at stacks.iop.org/2DM/9/015022/mmedia). We first studied the layer-dependent PL of thin WS_2 flakes (figure 1(a)) with thickness ranging from a monolayer (1L) to four layers (4L). Figure 1(b) shows the corresponding room-temperature PL maps of two WS_2 samples. We see that the monolayer portion of the WS_2 sample exhibits the strongest PL signal with a dramatic decrease in intensity as the thickness increases. This observation can be understood by the layer-dependent electronic structures of thin WS_2 layers, including (a) a transition from a direct (1L) to indirect (>1L) band gap; and (b) a reduced band gap as the sample thickness increases (see figure S2).

PVEs of the same samples were interrogated at room temperature (figure 1(a)) using SECCM (see figure 1(c)). In these studies, an electrochemical probe was constructed by filling a small (200–500 nm terminal diameter) conical probe with an aqueous electrolyte solution containing 100 mM NaI and 10 mM I_2. The inclusion of I^- and I_2 species creates a defined electrochemical potential within the probe based on the following reaction ($E^0 = 0.536$ V vs. standard hydrogen electrode $= -5.0$ eV vs. vacuum):

$$I_3^- + 2e^- \rightleftharpoons 3I^-$$

This probe was brought into contact with the sample, creating a miniaturized contact area between the sample and electrolyte solution. The effective area is defined by the size of the liquid meniscus which extends from the probe tip, which is typically ~1.5 times the physical dimensions of the probe. The tip diameter ranges from 200 to 500 nm, thus the corresponding effective area is between 7.1×10^{-14} and 4.4×10^{-13} m^2. The field within the sample can be controlled by applying a bias (V_b) between the ITO substrate and the electrochemical probe. Carriers driven to the sample-electrolyte interface can cross the interface by driving the above electrochemical reaction, resulting in a measurable current. In effect, the electrochemical probe in SECCM can behave as a reconfigurable, conformal contact with a work function effectively set by the electrolyte species. This approach has been recently applied to great effect in the study of photovoltaic processes in thick TMD layers [38–41]. It should also be noted that these SECCM measurements are non-destructive, which was confirmed through Raman analyses (see figure S3) carried out before and after PVE measurements and further supported by the high stability of photoelectrochemical solar cells made from these materials [42, 43].

PVEs in the TMD samples were investigated by obtaining a series of I–V curves with the probe in contact with an array of points spanning the structure of interest. During I–V measurements, samples were illuminated through the ITO substrate with a chopped broadband light source. Representative photocurrent maps obtained at $V_b = 0$ V for pristine WS_2 samples are shown in figure 1(d). In contrast to the PL results (figure 1(b)), the photocurrent of WS_2 increases with the increasing thickness (figure 1(d)). We further plotted the representative I–V curves taken from different regions of the WS_2 sample (figure 1(a)). As shown in figure 1(e), three essential features can be observed when V_b is larger than the open-circuit voltage (V_{OC}), including (a) the photocurrent with negligible dark current can be observed in all the layers; (b) the photocurrent gradually saturates as V_b increases to a higher value, indicating a clear photodiode behavior; and (c) the photocurrent ($V_b = 0$ V) increases with an increasing number of layers (inset of figure 1(e)), showing a strong layer-dependent photocurrent consistent with the mapping results shown in figure 1(d). On the other hand, when V_b is $<V_{OC}$, we only observed an apparent dark current in all the layers that quickly saturates. Such saturation is due to the diffusion-limited transport of I_3^- species to the interface. Meanwhile, we observed a small negative photocurrent when V_b is slightly smaller than V_{OC} that was quickly suppressed by the appearance of a dark current. Furthermore, important merits for photovoltaic devices, the corresponding open-circuit voltage V_{OC} and short-circuit current I_{SC} were extracted as listed in table S1. We find that I_{SC} decreases as the thickness of WS_2 decreases. Although the highest V_{OC} was observed in the monolayer WS_2, no clear layer-dependence of the V_{OC} can be identified.

To understand the I–V characteristics and photocurrent of the thin WS_2 layers, we applied band structure analysis based on metal-semiconductor junction physics. In the WS_2 device, two junctions are formed at the ITO/WS_2 and WS_2/electrolyte interfaces. Band offsets at these interfaces depend on the work function of the ITO and the electrochemical potential of the I_3^-/I^- redox couple. Simplified band

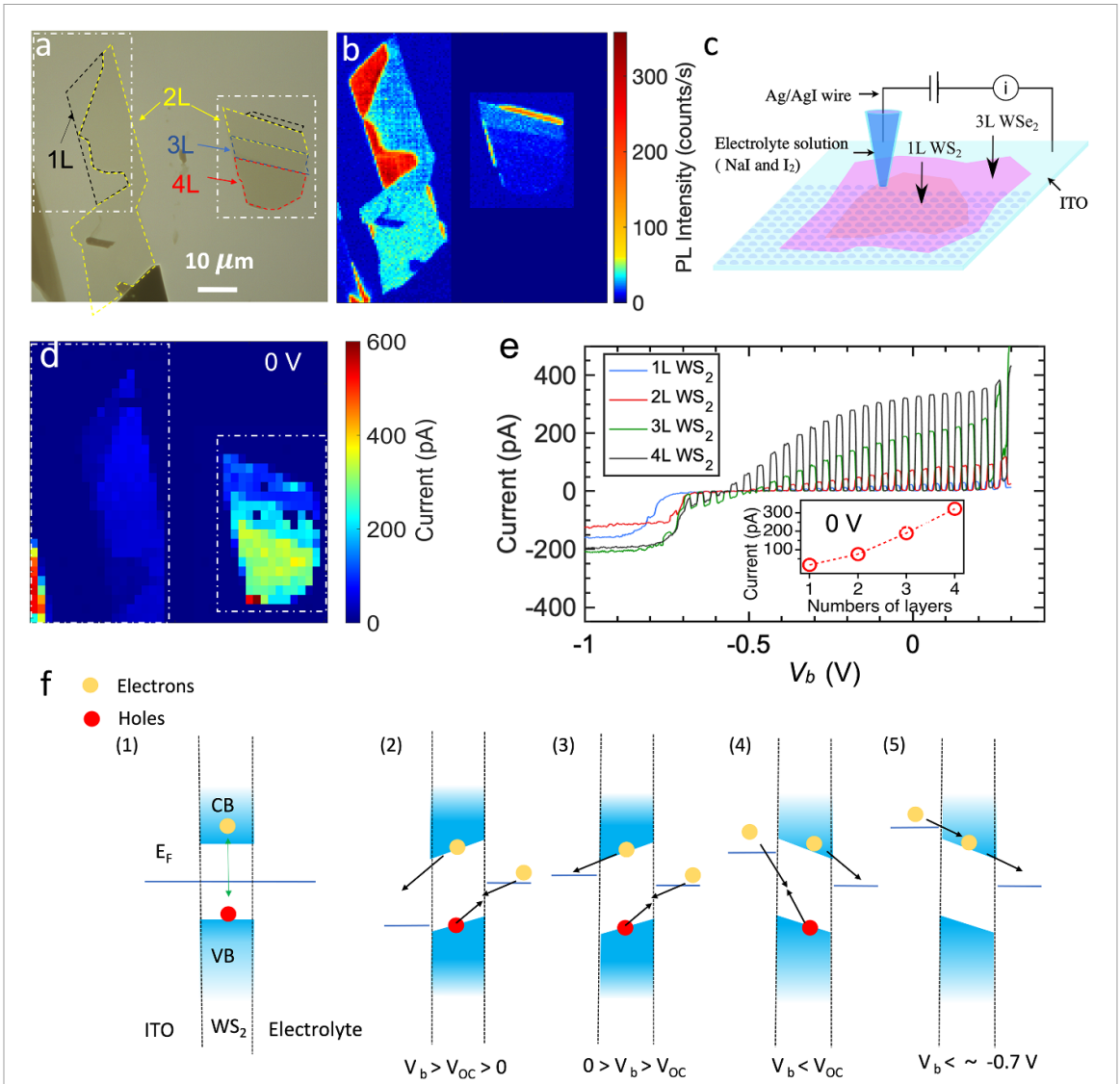

Figure 1. Layer-dependent PL and PVE of thin WS_2 layers. (a) An optical image of the WS_2 layers with different thicknesses on an ITO substrate. PL (b) map of the sample in (a), (c) schematic of the SECCM measurements. (d) Photocurrent map of the WS_2 samples in (a), (e) layer-dependent I–V characteristics of WS_2. Inset is the layer dependence of the photocurrent measured at a bias (V_b) of 0 V applied between the ITO substrate and the electrolyte. (f) Schematic band diagrams of WS_2 under different V_b's. (1) Band alignment at equilibrium state; (2) $V_b > V_{OC} > 0$; (3) $0 > V_b > V_{OC}$; (4) $V_b < V_{OC}$; (5) $V_b < \sim -0.7$ V.

diagrams of the device structure at different V_b's are shown in figure 1(f). At the equilibrium state, the Fermi level E_F is located near the middle of the band gap of WS_2 due to its intrinsic nature. Under optical excitation, electrons in the valence band (VB) can be excited to the conduction band (CB) where electron–hole pairs (EHPs) are generated, contributing to the photocurrent. When $V_b > V_{OC} > 0$, as shown in diagram (2) of figure 1(f), the energy bands of WS_2 near the ITO side is lowered. Under illumination, holes generated in the WS_2 layer flow towards the electrolyte interface, driving the oxidation of I^-. Meanwhile, the excited electrons in the CB of WS_2 are driven towards the ITO substrate, resulting in a positive photocurrent. Negligible dark current is expected since hole injection from ITO into the VB is unfavorable. When $0 > V_b > V_{OC}$, as shown in diagram (3) of figure 1(f), the Fermi level of ITO is lifted up to slightly higher than that of the electrolyte. However, a positive photocurrent is still expected because of the unchanged energy band bending in WS_2 induced by the generated EHPs. On the other hand, when V_b is $<V_{OC}$ (diagram (4) of figure 1(f)), the Fermi level of ITO is further lifted up to a point still lower than the CB of WS_2. Under illumination, the energy bands of WS_2 will be bent in the opposite direction. Thus, the excited electrons in CB of WS_2 are driven to the electrolyte and electrons in ITO recombine with holes in VB of WS_2, resulting in a negative photocurrent as observed in figure 1(e). When a more negative V_b is applied (about −0.7 V, diagram (5) of figure 1(f)) the Fermi level E_F of ITO is now higher than the CB of WS_2 and electrons can directly transfer from the ITO substrate to the electrolyte through the CB of WS_2, resulting in an apparent dark current and a negligible photocurrent, consistent with

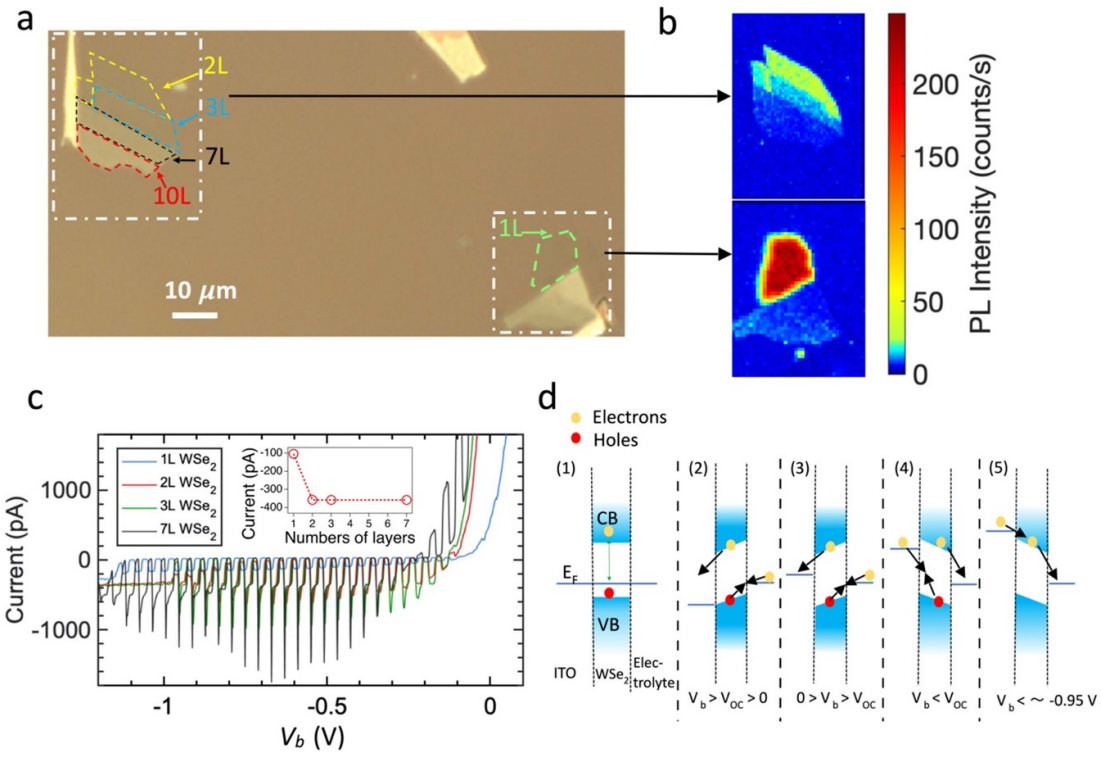

Figure 2. Layer-dependent PL and PVE of thin p-WSe_2 layers. (a) An optical image of WSe_2 layers with different thicknesses on an ITO substrate. (b) PL maps of WSe_2 samples in (a), (c) layer-dependent I–V characteristics of the thin WS_2 layers. Inset shows the layer dependence of the photocurrent measured at a bias (V_b) of −0.5 V between the ITO substrate and the electrolyte. (d) Schematic band diagrams for thin WSe_2 layers under different V_b's. (1): band alignment at equilibrium state; (2) $V_b > V_{OC} > 0$; (3) $0 > V_b > V_{OC}$; (4) $V_b < V_{OC}$; (5) $V_b < \sim -0.95$ V.

our experimental observations (figure 1(e)). We note that the layer dependence of PVEs for the thin WS_2 layers is different from previously reported results of MoS_2 [44] even though both samples have a similar layer-dependent PL behavior. In our case, the enhanced photocurrent in thicker WS_2 samples is mainly due to the reduced band gaps as well as the increased light absorption in thicker samples. When a white light source is applied the narrower the band gap results in a wider range of absorbed photon energies. Thus, more EHPs can be generated in thicker layers resulting in a higher photocurrent. We note that, since a laser source was used in the studies of previous MoS_2 samples [44], a direct comparison between the two experiments may not be straightforward.

2.2. Layer-dependent PL and PVE of p-type WSe_2

We performed similar PL and PVE measurements on thin p-type WSe_2 layers. Figure 2(b) shows the representative PL maps taken from two samples (marked by two white rectangles in figure 2(a)) with different thicknesses. Similar to WS_2, the PL signal decreases as the thickness of WSe_2 increases because both WS_2 and WSe_2 feature a similar layer-dependent direct to indirect energy gap transition (see figure S4). Figure 2(c) shows the I–V characteristics of the WSe_2 samples taken from different locations with different thicknesses (figure 2(a)). The layer-dependent photocurrent in p-type WSe_2 is more complex in contrast to WS_2. For instance, among the WSe_2 flakes, the thin ($\leqslant$4L) and thick flakes ($\geqslant$7L) show very different photovoltaic behaviors as shown in figures 2(c) and S5. For thicker flakes ($\geqslant$7L), both the photocurrent and dark currents can be observed when V_b is $>V_{OC}$ while the dark current remains high in the thinner layers, where the photocurrent is missing. When V_b is $<V_{OC}$, the photocurrent was detected in all the measured WSe_2 layers and is insensitive to the applied V_b whereas the dark current vanishes. Furthermore, when a more negative V_b is applied (<-0.9 V), an apparent dark current with a negligible photocurrent was detected in the thin layers (figures 2(c) and S5). We have depicted the photocurrent (at $V_b = -0.5$ V) as a function of the number of WSe_2 layers in the inset of figure 2(c) where the photocurrents of the measured layers greater than a monolayer are very close to 350 pA. Another prominent feature is the spikes in the I–V curves measured in 2, 3 and 7L samples. These spikes appear instantly when the light is on and then decay quickly. Such a feature is mainly due to charge recombination/trapping at the interface [45]. We note that in this study only the steady-state photocurrent is considered. We further analyzed the layer-dependences of both the V_{OC} and I_{SC} of the WSe_2 as listed in table S1, where both the V_{OC} and I_{SC} of WSe_2 decrease as the thickness decreases.

To qualitatively understand the PVE of p-type WSe_2, we consider the simplified band diagram of p-type WSe_2 devices at different V_b's, as shown in figure 2(d). At the equilibrium state (diagram (1) of figure 2(d)), the E_F is close to the VB of WSe_2 due to its p-type nature. When $V_b > V_{OC} > 0$ (diagram (2) of figure 2(d)), a significant dark current can flow through the devices (ITO /WSe_2/electrolyte) through the VB of WSe_2 consistent with our experimental observations as shown in figure 2(c). Under illumination, the generated EHPs further enhance the overall current resulting in a photocurrent. We note that the photocurrent is only detected in thick layers (see figures 2(c) and S5). When $0 > V_b > V_{OC}$ (diagram (3) of figure 2(d)), the band bending in WSe_2 still predicts a positive photocurrent but minimal dark current. We note that the positive photocurrent was only observed in our thick samples and an obvious dark current was observed in all the measured layers. Such a contradiction requires further study. When $V_b < V_{OC}$, as shown in diagram (4) of figure 2(d), the energy bands of the WSe_2 near the ITO interface are lifted up. In this case, no dark current is expected due to the energy barriers for both charge carriers at the interfaces while the photo-generated electrons in the CB of the WSe_2 can flow into the electrolyte contributing to a negative photocurrent that is consistent with our experimental observations. When the V_b is more negative (about −0.95 V as shown in diagram (5) of figure 2(d)) the Fermi level of the ITO is now above the CB edge of WSe_2. Therefore, electrons from ITO can directly travel to the electrolyte resulting in a significant dark current as observed in our thin samples (figures 2(d) and S5).

2.3. Layer-dependent PL and PVE of WSe_2/WS_2 vertical heterostructures

We further studied the layer-dependent PL and PVE of the WSe_2/WS_2 vertical heterostructures. Figure 3(a) shows a schematic of a WSe_2/WS_2 heterostructure (type-I) where a uniform WSe_2 layer sits on a WS_2 flake with different thicknesses at different locations. The optical image of an actual device (S1, with a 3L WSe_2 and a WS_2 flake containing 3, 4, 5, and 13L) is shown in figure 3(b) where different vertical heterojunctions can be formed. With such a configuration, measurements on all the formed heterojunctions can be performed under the same conditions, offering a direct way to compare their performance. Figures 3(c) and (d) show a PL map taken from the white rectangle region in figure 3(b) and a photocurrent map measured from the square region highlighted in figure 3(c) at $V_b = 0$ V, respectively. One can see that the PL signal is suppressed in all the heterojunction areas whereas the photocurrent is significantly enhanced. For instance, the photocurrent of a WSe_2 (3L)/WS_2 (3L) heterostructure (figure 3(g), measured at $V_b = 0.15$ V) has been enhanced by about 30 times compared to those from its constituents (3L WS_2 and 3L WSe_2). Such an enhancement is mainly due to enhanced charge transfer and exciton dissociation in the heterojunction[19]. Figures 3(e) and (f) show the representative I–V characteristics taken from samples S1 and S2, respectively. Two distinct features can be found from the layer-dependent I–V characteristics: (a) a significant dark current was observed in the 1L and 2L WS_2 (sample S2) while the dark current is absent from all other combinations when WS_2 is thicker than 2L. This is mainly due to a lower tunneling barrier in the junction with a thinner WS_2 layer compared with a thicker WS_2 layer; and (b) the photocurrent can only be observed when a V_b is larger than V_{OC} and decreases with the increasing thickness of WS_2. In figure 3(h) we summarized the layer-dependence of the photocurrents measured from both the constituent WS_2 (red right axis) and the heterostructure (blue left axis) regions from the two samples (S1 and S2).

One can see that, consistent with the data shown in figure 1(d), the photocurrent measured from pristine WS_2 layers increases as its thickness increases. However, in the junction region, the photocurrent first decreases with the increasing thickness of WS_2 and then slightly increases as the thickness of WS_2 reaches a threshold value. In addition, we compared the layer dependences of the V_{OC} and I_{SC} (table S1) of the heterostructures. In the same device, the V_{OC} stays unchanged as the thickness of the constituent WS_2 layer varies. We note that a slightly higher value of V_{OC} was observed in the 4L WSe_2/3L WS_2. The slight difference between different devices on different substrates may be due to the environmental effects and different measurement conditions. It is also noted that the short circuit current decreases as the thickness of the WS_2 layer increases.

To further study the role of the WSe_2 layer in the PL and PVE of the WSe_2/WS_2 vertical heterostructures, we fabricated a type-II heterostructure consisting of a WS_2 bottom layer with a fixed thickness and a WSe_2 top flake with different thicknesses at different locations (figure 4(a)). Figure 4(b) shows the optical image of such a WSe_2/WS_2 vertical heterostructure. The corresponding room-temperature PL map is shown figure 4(c), where the PL intensity is reduced in the heterojunction region. We note that, although the PL signal is still obvious in the junction regions of 1L (and 2L) WSe_2/4L WS_2, its intensity is already much lower than those taken from the pristine 1L and 2L WSe_2. Figure 4(d) shows the short circuit photocurrent map obtained from the sample shown in figure 4(b). One can see that the highest photocurrent was detected in the 4L WSe_2/4L WS_2 location. To analyze the layer-dependent PVE, the characteristic I–V curves taken from different locations of the device (figure 4(b)) are shown in figure 4(e). We further summarized the corresponding photocurrent ($V_b = 0$ V) as a function of the number of WSe_2 layers in figure 4(f). The photocurrents observed in all the

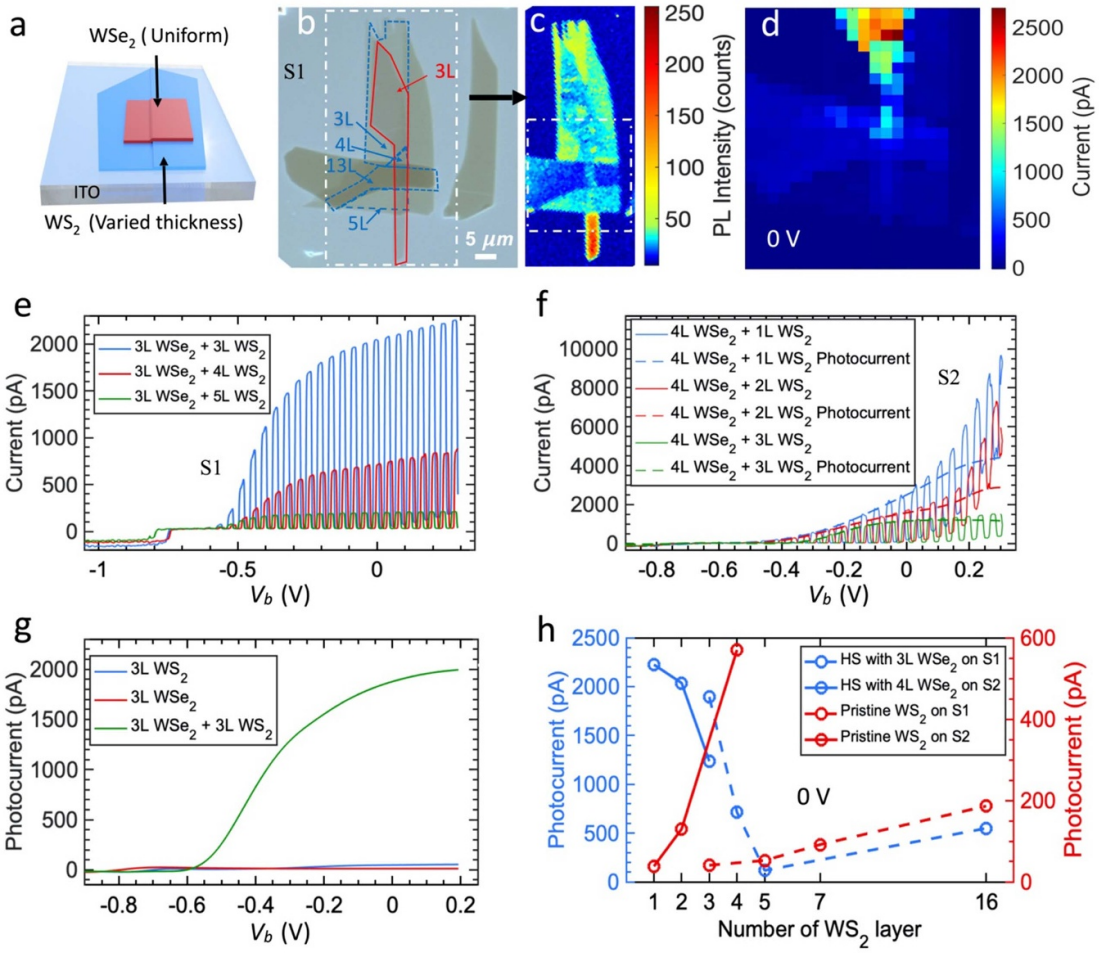

Figure 3. Layer-dependent PL and PVE of WSe_2 /WS_2 heterostructures with a fixed thickness of WSe_2. (a) Schematic of a vertically stacked WSe_2/WS_2 heterostructure with different thicknesses of WS_2 and a fixed thickness of WSe_2 on an ITO substrate. (b) An optical image of a WSe_2/WS_2 heterostructure (sample 1, *S1*). The contours of the 3, 4, 5 and 13L of WS_2 are highlighted by the blue dashed lines. The contour of the 3L WSe_2 is highlighted by the red lines. (c) A PL map of *S1* taken from the box in (b). (d) A photocurrent map of *S1* taken from the region highlighted by the white box in (c) at $V_b = 0$ V. Layer-dependent *I–V* characteristics of samples *S1* (e) and *S2* (f). The dashed lines in (f) represent the pure photocurrents taken from different locations of *S2*. (g) Photocurrents taken from different regions of a WSe_2 (3L) /WS_2 (3L) heterostructure, where the photocurrent has been enhanced by more than 30 times (at $V_b = 0.15$ V) in the WSe_2 (3L)/WS_2 (3L) junction region comparing with that of the pristine 3L WS_2 or WSe_2. (h) Photocurrent measured at $V_b = 0$ V as a function of the number of WS_2 layers in the WSe_2 /WS_2 heterostructures (right axis) and of the pristine WS_2 layers (left axis).

junctions increase as the thickness of the WSe_2 layers increases (figures 4(e) and (f)). We note that such a layer-dependent photocurrent is drastically different from that of WS_2 in the vertical heterostructures (figure 3(h)). In addition, we find that V_{OC} increases as the thickness of WSe_2 increases while the V_{OC} stayed unchanged as the thickness of WS_2 varies (table S1). The corresponding I_{SC} increases as the thickness of WSe_2 increases.

To explain the PVE observed in these WSe_2/WS_2 vertical heterostructures, we investigated the band diagram of ITO/WSe_2/WS_2/electrolyte junctions under different V_b's as shown in figure 5. Figure 5(a) shows the heterostructure at equilibrium. The band alignment between WS_2 and WSe_2 is known as type-II [46] that is consistent with our density functional theory (DFT) calculations (see figure S6). Under illumination, in addition to creating intralayer excitons within WSe_2 and WS_2, interlayer excitons can also be generated by exciting electrons from VB of WSe_2 to CB of WS_2. When the V_b is greater than V_{OC} and less than 0 V, as shown in the figure 5(b), the energy bands of the heterostructure near the ITO side are tilted down. Thus, under illumination, both intralayer and interlayer excitons can be generated in the vertical WSe_2/WS_2 heterostructures. Owing to the positive bias, the electrons from the electrolyte can recombine with the holes in the VBs of both WS_2 and WSe_2; meanwhile the photoexcited electrons in the CBs can travel to the ITO substrate resulting in a positive photocurrent. When $0\ V > V_b > V_{OC}$, as shown in figure 5(c), the Fermi level of the ITO is lifted up while the energy bands of the heterojunction are still bent in the same way as that of $V_b > V_{OC} > 0$. Thus, similar electron and hole transfer processes are expected. In the case of $V_b < V_{OC}$, the band bending

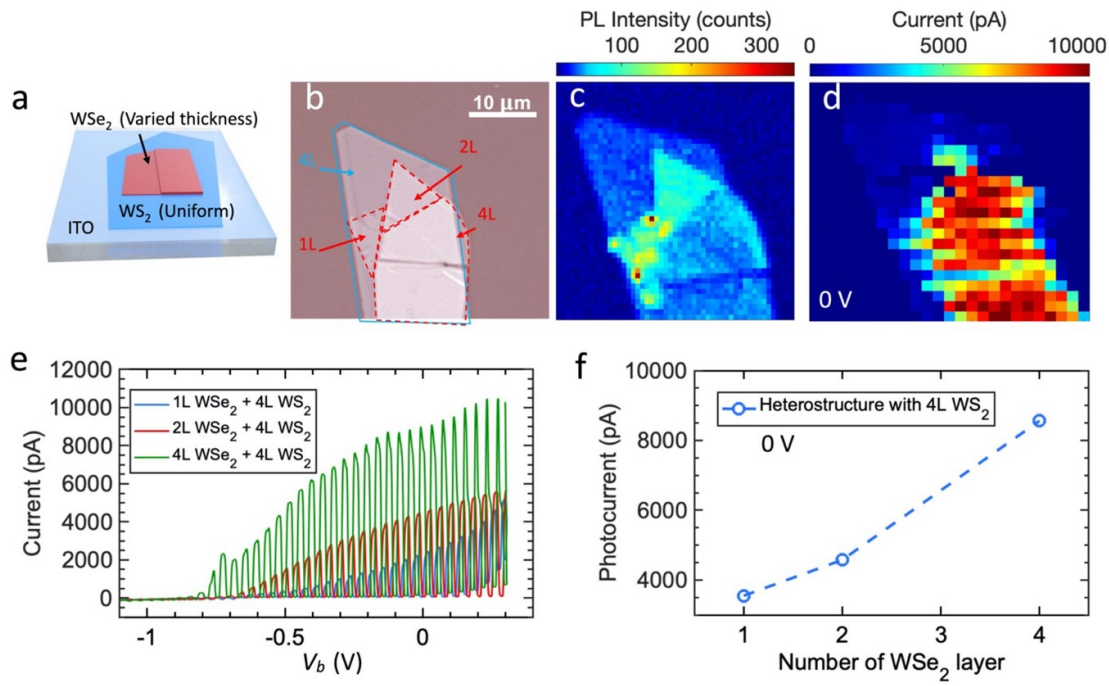

Figure 4. Layer-dependent PL and PVE of WSe_2/WS_2 heterostructures with a fixed thickness of WS_2. (a) Schematic of a WSe_2/WS_2 heterostructure with different thicknesses of WSe_2 and a fixed thickness of WS_2 on an ITO substrate. (b) An optical image of a WSe_2/WS_2 heterostructure. The contours of the top WSe_2 and bottom WS_2 are highlighted by the dashed green and blue lines, respectively. PL (c) and photocurrent (d) maps (at $V_b = 0$ V) of the sample in (b), (e) layer-dependent I–V characteristics of the sample in (b), (f) photocurrent (at $V_b = 0$ V) as a function of the number of WSe_2 layers in the WSe_2/WS_2 heterostructure.

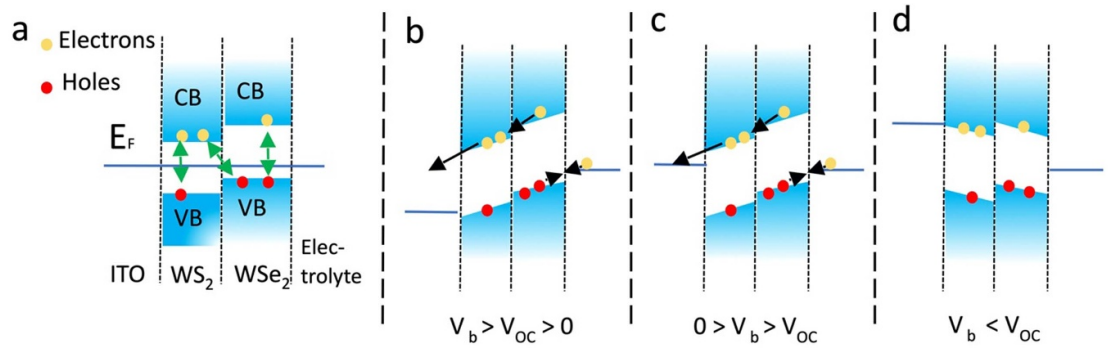

Figure 5. Band diagrams for WSe_2/WS_2 heterostructures. (a) Band alignment at equilibrium state; (b) $V_b > V_{OC} > 0$; (c) $0 > V_b > V_{OC}$; (d) $V_b < V_{OC}$.

in the heterojunction is now changed to the opposite direction as shown in figure 5(d). Owing to the energy barrier at the WSe_2/WS_2 interface, no charge carriers can flow across the entire junction, resulting in zero photo and dark currents. We note that all these expectations are consistent with our experimental observations.

We have demonstrated that the PL signal is significantly suppressed in the WSe_2/WS_2 vertical heterojunctions (figures 3, 4 and S7). To understand this phenomenon, we now focus on the simplest heterostructure of 1L WSe_2/1L WS_2 (figure S7). The PL signal is quenched in the junction region but retains a high intensity in the pristine WSe_2 and WS_2 areas since both of them feature a direct band gap. We also performed a band structure calculation of the 1L WSe_2/1L WS_2 heterojunction where an indirect band gap (figure S7(c)) is expected after considering the inter-layer interaction between the two constituents. Thus, we can conclude that, similar to multilayer WS_2 and WSe_2 samples, the mechanism of the suppressed PL in the WSe_2/WS_2 heterojunctions is mainly due to the transition from a direct to indirect band gap.

From our studies of the layer dependent PVE of the WSe_2/WS_2 heterostructure and its constituents, we noticed two anomalous behaviors for the WSe_2/WS_2 heterostructures: (a) the photocurrents in pure WS_2 flakes increase with increasing WS_2 thicknesses, whereas an opposite dependence of the

photocurrent on WS_2 layers was observed in the WSe_2/WS_2 heterostructure; and (b) the photocurrent in pristine WSe_2 is largely thickness-independent while the photocurrent in WSe_2/WS_2 heterostructures would increase with the increasing thickness of WSe_2. To address these anomalies, we propose a possible explanation based on the calculated band structures of the WSe_2/WS_2 heterostructures (figure S6). We find that the conduction band minimum (CBM) of WSe_2 moves to a higher energy and the CBM of WS_2 remains almost unchanged. With addition of 1L WS_2 onto the 1L WS_2/2L WSe_2 heterostructure, a larger band gap is expected in the WSe_2 side. Therefore, in the 2L WSe_2/2L WS_2 heterostructures, the energy range of the intra-band absorption spectrum of the WSe_2 layer is narrowed and fewer EHPs can be generated under white light illumination. On the other hand, when a WSe_2 monolayer is added to the 2L WS_2/1L WSe_2 heterostructure, both CBMs of WS_2 and WSe_2 are lowered. The corresponding energy ranges of the intra- and inter-band absorption spectra in the 2L WSe_2/2L WS_2 heterostructure can be expanded resulting in photocurrent enhancements, consistent with our experimental observations.

3. Conclusion

In summary, we have fabricated high-quality WS_2 and WSe_2 atomic layers and their vertical heterojunctions on ITO substrates and explored their layer-dependent photoresponses (including PVE and PL). In particular, we found that the photocurrent increases with the increasing thickness of the pristine WS_2 while the photocurrent in WSe_2 is largely independent on the sample thickness. For the vertical heterojunctions, we observed anomalous behavior of the layer-dependent photocurrents. For instance, the photocurrent decreases with increasing WS_2 thickness while an opposite layer dependence for the WSe_2 layer was observed. For the layer-dependent PL signals, we observed consistent results in all the samples meaning that the PL intensity is largely reduced as the band gap changes from direct to indirect. Our study provides a new understanding of 2D semiconductors and their heterostructures and paves new ways to optimize the performance of 2D-semiconductors-based photodetectors for possible energy-harvesting applications.

4. Methods

4.1. Materials and chemicals

NaI (Sigma Aldrich, $\geqslant$99%) and I_2 (Mallinckrodt, U.S.P grade) were obtained from the indicated sources and used without further purification. Ag wire (Alfa-Aesar, 0.25 mm, 99.99%) was employed as the counter electrode for probe fabrication, and stored in an aqueous solution containing 100 mM NaI and 10 mM I_2 when not in use. ITO-coated cover glass slides (22 $\times$ 22 mm, #1.5, 30–60 Ω sq., Structure Probe Inc (SPI)) were employed as sample substrates. Bulk WS_2 and WSe_2 crystals with dopant densities of $\sim 3 \times 10^{14}$ cm^{-3} and $\sim 2 \times 10^{17}$ cm^{-3}, respectively, were prepared via vapor transport methods [42, 43, 47]. The compositions of WS_2 and WSe_2 were confirmed by the energy-dispersive x-ray spectroscopy, as shown in figure S8.

4.2. Device fabrication

WSe_2 and WS_2 flakes were exfoliated on SiO_2 ($\sim$285 nm)/Si substrates. The WSe_2 and WS_2 layers with different thicknesses were first selected based on their optical contracts and then identified by atomic force microscopy. The targeting WSe_2 or WS_2 thin layers were picked up using a polyvinyl alcohol coated Polydimethylsiloxane stamp and then transferred onto ITO substrates using a dry-transfer method. The WSe_2/WS_2 heterostructures were fabricated using the same dry-transfer method. We note that all the transfer processes were carried out inside a gloves box with both the H_2O and O_2 levels below 0.1 ppm. A detailed illustration of the transfer process can be found in figure S1. The samples were annealed in a vacuum (<5 mTorr) at 230 °C for 3 h.

4.3. Probe fabrication

Pipet-based electrochemical probes were fabricated from quartz capillaries (1.2 mm outer diameter, 0.9 mm inner diameter, Sutter) using a laser-based pipet puller (Sutter P-2000). Probes were fabricated using a two-line program: Heat = 750, Fil = 4, Vel = 30, Delay = 135, Pull = 80/Heat = 685, Fil = 3, Vel = 30, Delay = 135, Pull = 150. These probes were filled with an aqueous electrolyte solution containing 100 mM NaI and 10 mM I_2, and a AgI-coated Ag wire was inserted into the back of the pipet, completing the electrochemical probe. The Ag/AgI wire provided a well-defined reference potential in the electrolyte corresponding to the $AgI + e^- \rightarrow Ag + I^-$ couple, and all data presented herein is referenced vs this potential.

4.4. PL measurements

For PL mapping, samples were mounted on a 2-axis piezoelectric stage (PI P546.2C7) of an inverted optical microscope. The sample was illuminated with a pulsed laser source (485 nm, FWHM $\approx$ 110 ps, Picoquant) focused through a microscope objective (100×, NA = 0.9). PL from a localized region of the sample was collected using the same objective and directed through a non-polarizing beam splitter. One beam was directed onto the slit of a spectrometer-charge coupled device (CCD) combination (Andor SR-303i-B, Newton EMCCD) and the other onto an avalanche photodiode micro photon devices (MPD) connected to a TCSPC system (Picoquant Picoharp 300). All instrumentation was controlled through

custom LabVIEW software. For the PL spectra acquisition, a Horiba confocal Raman microscope with 532 nm laser excitation was employed.

4.5. SECCM measurements

Samples were mounted on ceramic slides and placed on the stage of an inverted optical microscope. Electrical contact to the sample was made using Cu tape. The electrochemical probe was mounted to a three-axis piezoelectric stage (PI P-611.3S). A patch-clamp style amplifier (Dagan CHEM-CLAMP) was employed to provide electrical bias between the sample and Ag/AgI counter electrode (ground). The sample was placed under intermittent (50 Hz) broadband illumination (50 W cm^{-2}, Energetiq LDLS) and the electrochemical probe was lowered towards the sample, while a potential difference of −0.5 V was applied to the substrate and the current flowing in the system was monitored. Probe-sample contact was identified by a sudden current spike. Once the contact was established, probe movement was stopped and a triangular potential waveform (2000 mV s^{-1}) was applied while the resulting currents were recorded. Upon completion of the waveform, the probe was retracted and moved laterally, where this procedure was repeated. Measurements were taken across a rectangular array of points and current data were recorded as a three-dimensional array. All instrumentation was controlled through custom LabVIEW software and a National Instruments DAQ interface (cDAQ-9174). Photocurrent images and voltammograms at specific points were generated from the raw data via custom python scripts.

4.6. Raman spectroscopy

The Raman spectra were acquired under ambient conditions by a Horiba confocal Raman microscope with a 532 nm laser excitation. A 2400 grooves mm^{-1} grating was used to achieve a spectral resolution of below 1.4 cm^{-1}.

4.7. DFT calculations

The electronic structures of the WSe_2 and WS_2 layers were calculated using a plane wave implementation of DFT in Quantum Espresso [48–50]. We engaged the 2 H stacking in multilayer cases as it is found to be the most stable structure. The lattice constants used in the calculations are consistent with experimental data [51]. A vacuum of at least 20 Å was used along the *z*-direction to minimize the interaction among the periodic images. Projected augmented wave (PAW) potentials were used to self-consistently solve the electronic structure with a k-point mesh of 12 × 12 × 1. The cut-off energies for the plane-wave basis states were 60 Ry. The Per-Burke-Ernzerhof (PBE) approximation was used for the exchange-correlation function. The weak van der Waals interaction was included by using a dispersion correction based on Grimme's DFT-D2 method [52, 53].

The WSe_2 /WS_2 heterostructures were constructed with 2H stacking as shown in figures S7(a) and (b). The distance *d* between WSe_2 and WS_2 which is defined as the distance between neighboring W atom's planes as shown in figure S6(a), was determined by geometry optimization as listed in figure S6(c). The other lattice constants of the heterostructures were kept identical with that of WS_2. The geometry was optimized using the Broyden-Fletcher-Goldfarb-Shenno minimization technique, with a threshold of the converged structure of energy change per atom smaller than 1.6 × 10^{-4} Ry/atom. The vacuum spacer (larger than 15 Å) was used for all the heterostructures. PAW potentials were used to self-consistently solve the electronic structure with a k-point mesh of 12 × 12 × 1. The cut-off energy for the plane-wave basis states was 80 Ry. PBE approximation was used for the exchange-correlation functional. The weak van der Waals interaction was included by a dispersion correction based on the Grimme's DFT-D2 method. We calculated the orbital projected band structures using the Quantum espresso and Wannier90 [54, 55]. We note that the spin–orbital interaction was not included in all calculations.

Data availability statement

The data that support the findings of this study are available upon reasonable request from the authors.

Acknowledgments

This research was supported by the U.S. Department of Energy, Office of Basic Energy Sciences, Division of Materials Sciences and Engineering (Project No. DE-SC0021281), Wyoming NASA EPSCoR (Project No. 80NSSC19M0061), the National Science Foundation (CHE-2045593), and the Wyoming NASA Space Grant Consortium (NASA Grant #NNX15AI08H). The calculations were supported by Advanced Research Computing Center, Teton Computing Environment at University of Wyoming.

ORCID iD

Jifa Tian https://orcid.org/0000-0003-2921-470X

References

[1] Britnell L *et al* 2013 Strong light-matter interactions in heterostructures of atomically thin films *Science* **340** 1311–4
[2] Lee H S *et al* 2012 MoS_2 nanosheet phototransistors with thickness-modulated optical energy gap *Nano Lett.* **12** 3695–700

[3] Lopez-Sanchez O, Lembke D, Kayci M, Radenovic A and Kis A 2013 Ultrasensitive photodetectors based on monolayer MoS_2 *Nat. Nanotechnol.* **8** 497–501
[4] Tsai D S *et al* 2013 Few-layer MoS_2 with high broadband photogain and fast optical switching for use in harsh environments *ACS Nano* **7** 3905–11
[5] Withers F *et al* 2015 Light-emitting diodes by band-structure engineering in van der Waals heterostructures *Nat. Mater.* **14** 301–6
[6] Ross J S *et al* 2014 Electrically tunable excitonic light-emitting diodes based on monolayer WSe_2 p–n junctions *Nat. Nanotechnol.* **9** 268–72
[7] Mak K F, McGill K L, Park J and McEuen P L 2014 The valley Hall effect in MoS_2 transistors *Science* **344** 1489–92
[8] Mak K F, Lee C, Hone J, Shan J and Heinz T F 2010 Atomically thin MoS_2: a new direct-gap semiconductor *Phys. Rev. Lett.* **105** 2–5
[9] Xue H *et al* 2019 High photoresponsivity and broadband photodetection with a band-engineered WSe_2 /$SnSe_2$ heterostructure *Nanoscale* **11** 3240
[10] Huo N, Kang J, Wei Z, Li S-S, Li J and Wei S-H 2014 Novel and enhanced optoelectronic performances of multilayer MoS_2–WS_2 heterostructure transistors *Adv. Funct. Mater.* **24** 7025–31
[11] Xia J *et al* 2021 Strong coupling and pressure engineering in WSe_2–$MoSe_2$ heterobilayers *Nat. Phys.* **17** 92–98
[12] Furchi M M, Pospischil A, Libisch F, Burgdörfer J and Mueller T 2014 Photovoltaic effect in an electrically tunable van der Waals heterojunction *Nano Lett.* **14** 4785–91
[13] Gong C, Zhang H, Wang W, Colombo L, Wallace R M and Cho K 2013 Band alignment of two-dimensional transition metal dichalcogenides: application in tunnel field effect transistors *Appl. Phys. Lett.* **103** 053513
[14] Zhao W, Ghorannevis Z, Chu L, Toh M, Kloc C, Tan P-H and Eda G 2013 Evolution of electronic structure in atomically thin sheets of WS_2 and WSe_2 *ACS Nano* **7** 791–7
[15] Geim A K and Grigorieva I V 2013 Van der Waals heterostructures *Nature* **499** 419–25
[16] Tran K *et al* 2019 Evidence for moiré excitons in van der Waals heterostructures *Nature* **567** 71–75
[17] Jin C *et al* 2019 Observation of moiré excitons in WSe_2/WS_2 heterostructure superlattices *Nature* **567** 76–80
[18] Alexeev E M *et al* 2019 Resonantly hybridized excitons in moiré superlattices in van der Waals heterostructures *Nature* **567** 81–86
[19] Lee C H *et al* 2014 Atomically thin p–n junctions with van der Waals heterointerfaces *Nat. Nanotechnol.* **9** 676–81
[20] Tsai M L *et al* 2017 Single atomically sharp lateral monolayer p–n heterojunction solar cells with extraordinarily high power conversion efficiency *Adv. Mater.* **29** 1701168
[21] Deng Y *et al* 2014 Black phosphorus-monolayer MoS_2 van der Waals heterojunction p–n diode *ACS Nano* **8** 8292–9
[22] Lee G, Pearton S J, Ren F and Kim J 2018 Two-dimensionally layered p-black phosphorus/n-MoS2/p-black phosphorus heterojunctions *ACS Appl. Mater. Interfaces* **10** 10347–52
[23] Zhang K *et al* 2016 Interlayer transition and infrared photodetection in atomically thin type-II $MoTe_2$/MoS_2 van der Waals heterostructures *ACS Nano* **10** 3852–8
[24] Wu E, Xie Y, Liu Q, Hu X, Liu J, Zhang D and Zhou C 2019 Photoinduced doping to enable tunable and high-performance anti-ambipolar $MoTe_2$/MoS_2 heterotransistors *ACS Nano* **13** 5430–8
[25] Zhou X *et al* 2018 Tunneling diode based on WSe_2/SnS_2 heterostructure incorporating high detectivity and responsivity *Adv. Mater.* **30** 1703286
[26] Yang T *et al* 2017 Van der Waals epitaxial growth and optoelectronics of large-scale WSe_2/SnS_2 vertical bilayer p–n junctions *Nat. Commun.* **8** 1–9
[27] Wong J *et al* 2017 High photovoltaic quantum efficiency in ultrathin van der Waals heterostructures *ACS Nano* **11** 7230–40
[28] Mefford J T *et al* 2021 Correlative operando microscopy of oxygen evolution electrocatalysts *Nature* **593** 67–73
[29] Wahab O J, Kang M and Unwin P R 2020 Scanning electrochemical cell microscopy: a natural technique for single entity electrochemistry *Curr. Opin. Electrochem.* **22** 120–8
[30] Daviddi E *et al* 2019 Nanoscale visualization and multiscale electrochemical analysis of conductive polymer electrodes *ACS Nano* **13** 13271–84
[31] Bentley C L, Edmondson J, Meloni G N, Perry D, Shkirskiy V and Unwin P R 2019 Nanoscale electrochemical mapping *Anal. Chem.* **91** 84–108
[32] Kang M, Perry D, Bentley C L, West G, Page A and Unwin P R 2017 Simultaneous topography and reaction flux mapping at and around electrocatalytic nanoparticles *ACS Nano* **11** 9525–35
[33] Bentley C L, Kang M and Unwin P R 2017 Nanoscale structure dynamics within electrocatalytic materials *J. Am. Chem. Soc.* **139** 16813–21
[34] Aaronson B D B, Byers J C, Colburn A W, McKelvey K and Unwin P R 2015 Scanning electrochemical cell microscopy platform for ultrasensitive photoelectrochemical imaging *Anal. Chem.* **87** 4129–33
[35] Güell A G *et al* 2014 Mapping nanoscale electrochemistry of individual single-walled carbon nanotubes *Nano Lett.* **14** 220–4
[36] Snowden M E *et al* 2012 Scanning electrochemical cell microscopy: theory and experiment for quantitative high resolution spatially-resolved voltammetry and simultaneous ion-conductance measurements *Anal. Chem.* **84** 2483–91
[37] Castellanos-Gomez A *et al* 2014 Deterministic transfer of two-dimensional materials by all-dry viscoelastic stamping *2D Mater.* **1** 011002
[38] Hill J W and Hill C M 2021 Directly visualizing carrier transport and recombination at individual defects within 2D semiconductors *Chem. Sci.* **12** 5102–12
[39] Hill J W, Fu Z, Tian J and Hill C M 2020 Locally engineering and interrogating the photoelectrochemical behavior of defects in transition metal dichalcogenides *J. Phys. Chem.* C **124** 17141–9
[40] Strange L E *et al* 2020 Investigating the redox properties of two-dimensional MoS_2 using photoluminescence spectroelectrochemistry and scanning electrochemical cell microscopy *J. Phys. Chem. Lett.* **11** 3488–94
[41] Hill J W and Hill C M 2019 Directly mapping photoelectrochemical behavior within individual transition metal dichalcogenide nanosheets *Nano Lett.* **19** 5710–6
[42] Kline G, Kam K K, Ziegler R and Parkinson B A 1982 Further studies of the photoelectrochemical properties of the group VI transition metal dichalcogenides *Solar Energy Mater.* **6** 337–50
[43] Kline G, Kam K, Canfield D and Parkinson B A 1981 Efficient and stable photoelectrochemical cells constructed with WSe_2 and $MoSe_2$ photoanodes *Solar Energy Mater.* **4** 301–8
[44] Son Y *et al* 2015 Layer number dependence of MoS_2 photoconductivity using photocurrent spectral atomic force microscopic imaging *ACS Nano* **9** 2843–55
[45] Peter L M 1990 Dynamic aspects of semiconductor photoelectrochemistry *Chem. Rev.* **90** 753–69
[46] Kang J, Tongay S, Zhou J, Li J and Wu J 2013 Band offsets and heterostructures of two-dimensional semiconductors *Appl. Phys. Lett.* **102** 012111
[47] Prybyla S, Struve W S and Parkinson B A 1984 Transient photocurrents in WSe_2 and $MoSe_2$ photoanodes *J. Electrochem. Soc.* **131** 1587–94
[48] Enkovaara J, Rostgaard C and Mortensen J J 2017 Advanced capabilities for materials modelling with quantum ESPRESSO *J. Phys.: Condens. Matter* **29** 465901
[49] Giannozzi P *et al* 2009 QUANTUM ESPRESSO: a modular and open-source software project for quantum simulations of materials *J. Phys.: Condens. Matter* **21** 395502

[50] Giannozzi P et al 2020 Quantum ESPRESSO toward the exascale J. Chem. Phys. 152 154105
[51] Schutte W J, de Boer J L and Jellinek F 1987 Crystal structures of tungsten disulfide and diselenide J. Solid State Chem. 70 207–9
[52] Grimme S 2006 Semiempirical GGA-type density functional constructed with a long-range dispersion correction J. Comput. Chem. 27 1787–99
[53] Barone V et al 2009 Role and effective treatment of dispersive forces in materials: polyethylene and graphite crystals as test cases J. Comput. Chem. 30 934–9
[54] Pizzi G et al 2020 Wannier90 as a community code: new features and applications J. Phys.: Condens. Matter 32 165902
[55] Mostofi A A, Yates J R, Pizzi G, Lee Y-S, Souza I, Vanderbilt D and Marzari N 2014 An updated version of wannier90: a tool for obtaining maximally-localised wannier functions Comput. Phys. Commun. 185 2309–10